ChemComm

# Main Group Elements in the Electrochemical Proton and Carbon Dioxide Reduction



| | |
|---|---|
| Journal: | *ChemComm* |
| Manuscript ID | CC-FEA-07-2023-003606.R1 |
| Article Type: | Feature Article |
| | |

ARTICLE

# Main Group Elements in the Electrochemical Proton and Carbon Dioxide Reduction

Received 00th January 20xx,
Accepted 00th January 20xx

DOI: 10.1039/x0xx00000x

Soumalya Sinha,[a] and Jianbing "Jimmy" Jiang*[a]

Main-group elements are renowned for their versatile reactivities in organometallic chemistry, including $CO_2$ insertion and $H_2$ activation. However, electrocatalysts comprising a main-group element active site have not yet been widely developed for activating $CO_2$ or producing $H_2$. Recently, research has focused on main-group element-based electrocatalysts that are active in redox systems related to fuel-forming reactions. These studies have determined that the catalytic performances of heavier main-group element-based electrocatalysts are often similar to those of transition-metal-based electrocatalysts. Our group has recently reported the scope of including the main-group elements in the design of molecular catalysts and explored their applications in redox catalysis, such as the generation of $H_2$ upon coupling of two protons ($H^+$) and two electrons ($e^-$). This feature article summarizes our research efforts in developing molecular electrocatalysts comprising main-group elements at their active sites. Furthermore, we highlight their influence on the rate-determining step, thereby enhancing the reaction rate and product selectivity for multi-$H^+$/multi-$e^-$ transfer catalysis. Particularly, we focus on the performance of our recently reported molecular Sn- or Sb-centered macrocycles for electrocatalytic $H_2$ evolution reaction (HER) and on how their mechanisms resemble those of transition-metal-based electrocatalysts. Moreover, we discuss $CO_2$ reduction reaction ($CO_2$RR), another promising fuel-forming reaction, and emphasize the recent progress in including the main-group elements in the $CO_2$RR. Although the main-group elements are found at the active sites of the molecular catalysts and are embedded in the electrode materials for studying the HER, molecular catalysts bearing main-group elements are not commonly used for $CO_2$RR. However, the main-group elements assist the $CO_2$RR by acting as co-catalysts. For example, alkali and alkaline earth metal ions (e.g., $Li^+$, $Na^+$, $K^+$, $Rb^+$, $Cs^+$, $Mg^{2+}$, $Ca^{2+}$, and $Ba^{2+}$) are known for their Lewis acidities, which influence the thermodynamic landscape of the $CO_2$RR and product selectivity. In contrast, the elements in Groups 13, 14, and 15 are primarily used as dopants in the preparation of catalytic materials. Overall, this article identifies main-group element-based molecular electrocatalysts and materials for HER and $CO_2$RR.

## Introduction

New findings for main-group element-based catalysts have changed the perception that main-group elements cannot behave similar to transition metals in catalysis. However, the development of electrocatalysts comprising main-group elements, particularly molecular electrocatalysts with a main-group element at the active center, is uncommon. The difference in the orbital energy levels is a challenge that renders it difficult for main-group element-based catalysts to compete with transition-metal-based catalysts. For main-group compounds, a high-energy gap exists in their valence *s*- or *p*-orbitals, whereas the valence *d*-orbitals in transition metals are relatively less energetic, which typically enables the transition-metal active site to interact with small molecular substrates (e.g., $CO_2$, $H_2$, and $O_2$). Additionally, the valence *s*- or *p*-orbitals are often fully occupied, thus lacking vacant sites for the catalyst–substrate interactions. However, heavier main-group elements, such as Al, Sn, and Sb, have larger covalent radii than their lighter counterparts, such as B, C, and N, and can attain higher coordination numbers in their complexes. Consequently, the inclusion of heavier main-group elements has gained recognition in catalyst design for small-molecule activation.[1] Moreover, elements in Groups 1 and 2 have been influential in multi-proton ($H^+$) and multi-electron ($e^-$) redox catalysis, and typically promote catalysis by enhancing reaction kinetics.[2–4]

Molecular electrocatalysts are great platforms to understand the structure-function relationship, but the current research desires more catalytic materials upon immobilizing the molecular catalyst. Although strategies to immobilize molecular catalysts on the electrode surface have been reported,[5,6] molecular catalysts bearing main-group elements at the active center are rarely known. The applications of main-group complexes in molecular electrocatalysis are also rare. Recently, our group has sought to include main-group elements in the design of molecular electrocatalysts. For example, we have reported molecular Sn- or Sb-centered macrocycles that couple multi-$H^+$ and multi-$e^-$ to generate $H_2$ electrocatalytically.[7,8] We have also investigated the electrochemical mechanism of these Sn or Sb complexes toward the $H_2$ evolution reaction (HER), supported by computational calculations. This article includes

[a] *Department of Chemistry, University of Cincinnati, P.O. Box 210172, Cincinnati, Ohio 45221, United States.*
Corresponding author: Email: jianbing.jiang@uc.edu.

our contributions toward the design of main-group element-centered electrocatalysts and their performance in the electrocatalytic HER. Furthermore, we emphasize the work of others in the electrocatalytic HER using main-group elements to highlight recent progress in this field.

We believe that main-group element-based electrocatalysts could be promising for the efficient $CO_2$ reduction reaction ($CO_2RR$). Finding robust and efficient $CO_2RR$ catalysts has been of great interest, owing to their ability to mitigate atmospheric $CO_2$.[9–11] However, most catalyst designs rely on transition metals. In 2010, Ménard and Stephen reported that $CO_2$ could be reduced to methanol ($CH_3OH$) using an $(Mes)_3P(CO_2)(AlX_3)_2$ complex, where Mes is a mesitylene group and X is a bromide or chloride.[12] They revealed that Al-based frustrated Lewis pairs (FLP) are the important factors in $CO_2RR$ chemistry. Inspired by these results, several FLP-based main-group complexes have been explored for the $CO_2RR$, and the most common product observed was formate ($HCO_2^-$).[13] Another example of the electrochemical $CO_2RR$ using main-group-based FLP was reported by Thompson and Heiden, where an FLP supported $CO_2$ insertion into a main-group hydride bond while reducing $CO_2$ electrochemically.[14] They also investigated the effects of Lewis acids on the reactivity of $CO_2$ insertion into the main-group hydride bond by comparing the activities of seven Lewis acids, $[PhSiH_2]^+$, $[SiEt_3]^+$, $B(C_6F_5)_3$, $B(C_6F_5)_2Ph$, $B(C_6F_5)Ph_2$, $BPh_3$, and $BEt_3$, where Ph and Et denote phenyl and ethyl groups, respectively. The authors noted that stronger Lewis acids, such as $B(C_6F_5)_3$, became poor hydride donors to $CO_2$ upon forming a metal–hydride bond, such as $[HB(C_6F_5)_3]^-$. Furthermore, Lewis acids from Groups 1 and 2, as well as transition-metal-based catalysts, assisted in controlling the $CO_2RR$ selectivity and kinetics under electrochemical conditions, and we include this discussion later. In addition to the Lewis acid effects of the main-group elements, we highlight examples wherein they act as dopants when incorporated into electrode materials for the $CO_2RR$. Overall, this article presents examples of the main-group element-assisted electrochemical HER and $CO_2RR$, including recent reports from our group.

### Main group elements at catalytic site

To our knowledge, extremely few main-group elements serve as the active sites of catalysts for the electrochemical HER or $CO_2RR$. Al, Ga, Sn, Sb, and Bi have been used as catalyst active sites while performing electrochemical HER. To date, no main-group elements have been explored as the active center of the electrocatalyst for $CO_2RR$ In this section, we focus only on the main-group elements used as molecular HER electrocatalysts and summarize their roles in the electrochemical mechanisms.

**Al:** The second element in group 13, Al has rarely been used in electrocatalysis, except for two unique examples of Al(III) complexes that promote the HER, as reported by Berben et al.[15,16] They synthesized two Al(III) complexes chelated with a redox-active ligand, phenyl-substituted bis(imino)pyridine (**Al–BIP**, Fig. 1A) or bis(pyrazolyl)pyridine (**Al–BPP**, Fig. 1B), and studied their activities for $H_2$ production. The electrochemical HER studies were performed by dissolving these Al(III) complexes in tetrahydrofuran (THF) with a tetrabutylammonium hexafluorophosphate ($^nBu_4NPF_6$) electrolyte in the presence of a Brønsted acid, which supplied multiple $H^+$. Under these electrochemical conditions, a Faradaic efficiency (FE) of 85% for $H_2$ production was observed using **Al–BIP** in the presence of 4-dimethylaminopyridinium ($HDMAP^+$, 20 equiv.) by performing controlled potential electrolysis for 1.5 h at an overpotential of 0.5

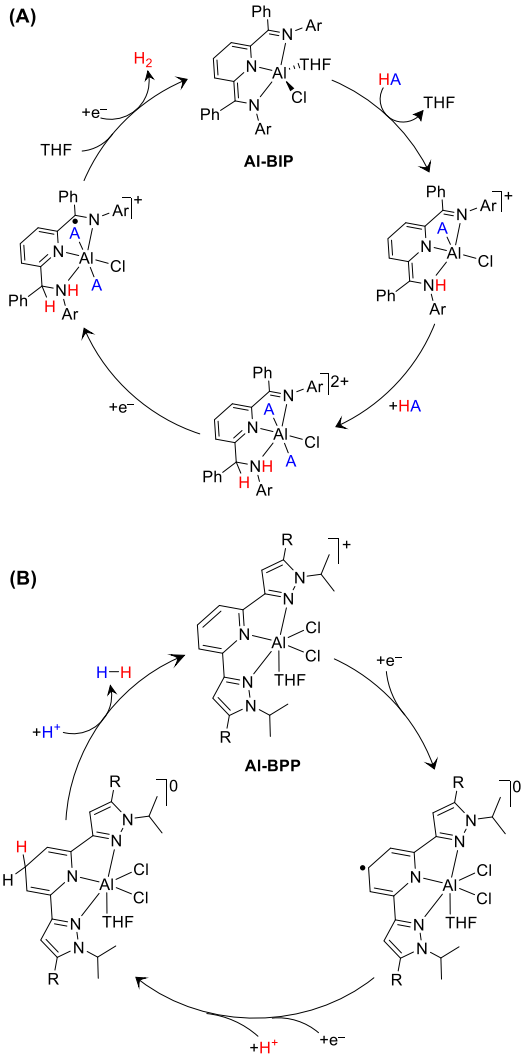


**Fig. 1.** Two different electrochemical HER pathways promoted by Al(III) complexes, (A) **Al–BIP** and (B) **Al–BPP**, coordinated with a redox-active ligand. HA is $HDMAP^+$. Adapted with the permissions of Refs. 15 and 16.

V. The electrochemical HER mechanism of **Al–BIP** was also studied, and it was proposed that two sequential proton transfers first occurred at the ligand center (Fig. 1A). The protonated **BIP** ligand (by $2H^+$) in **Al–BIP** underwent two further sequential $1e^-$ reduction steps to generate $H_2$ (Fig. 1A).

A similar electrochemical HER performance was observed for **Al–BPP** using triethylammonium ($[HNEt_3]^+$) or salicylic acid as the proton source in the THF electrolyte;[16] however, **Al–BPP** followed a slightly different electrochemical HER pathway (Fig. 1B). The **BPP** ligand in **Al-BPP** was first reduced by $1e^-$, and a proton-coupled electron transfer step occurred at the **BPP** ligand. Finally, $1H^+$ reduction generated $H_2$ (Fig. 1B). Detailed electrochemical data analysis

revealed that Al(III) did not participate in $H^+$ and $e^-$ transfer events. The supported redox-active ligand underwent sequential $H^+/e^-$ reduction to form a ligand-based hydride intermediate, which released $H_2$ in the presence of acids in the solution. Notably, both HER pathways promoted by **Al–BIP** and **Al–BPP** proceeded without forming any typical metal–hydride intermediates, which is common in transition-metal-centered HER electrocatalysts.[17–19] Overall, this research effort inspired a main-group-based molecular electrocatalyst design for HER catalysis.

**Ga:** Cao et al. reported a remarkable HER using Ga(III) chloride tetrakis(pentafluorophenyl)porphyrin (**ClGa$^{III}$TPF$_5$**, Fig. 2A).[20] In their study, the authors proposed that a Ga(III) porphyrin derivative promoted $H_2$ production, where the ligated porphyrin was first reduced consecutively by $2e^-$, followed by a Ga(III)–hydride species formation (Fig. 2B) using $H^+$ from the added acid source, 2,2,2-trifluoroacetic (TFA). A signal at –6.45 ppm in the $^1$H NMR spectrum confirmed the formation of the Ga(III)–hydride intermediate. In addition to NMR spectroscopy data, UV-visible spectroscopic studies were also carried out for the further detection of $1e^-$ or $2e^-$ reduced species of **ClGa$^{III}$TPF$_5$**. Interestingly, a weak absorption band between 560–700 nm appeared when Ga$^{III}$–hydride species was formed after the reaction between $2e^-$ reduced **ClGa$^{III}$TPF$_5$** species and added acids (AcOH or TFA). Furthermore, such experiments also supported the hypothesis that protonation events during the HER process take place at the Ga$^{III}$ center rather than at the *meso*-position of the porphyrin ring. Finally, further protonation of the Ga(III)–hydride intermediate using Brønsted acids resulted in $H_2$ production. A turnover frequency (TOF) of $9.4 \times 10^4$ s$^{-1}$ was estimated for the HER using this molecular Ga(III) porphyrin catalyst in $CH_3CN$ with TFA (97 equiv.). Moreover, the HER kinetics observed using this Ga(III) porphyrin catalyst were much higher than those of the Sb(III)-porphyrin-derived catalysts. This phenomenon could be rationalized by considering the stronger hydride-donating ability of the Ga(III)-based hydride than that for the Sb(III)-based hydride, owing to the smaller electronegativity of Ga.[20]

**Sn:** Motivated by the performance of Ga(III) and Sb(III) porphyrins toward electrochemical HER, we recently reported an asymmetric PEGylated Sn(IV) porphyrin (**Cl$_2$Sn$^{IV}$PEGP**, Fig. 3A) for homogeneous HER in a non-aqueous electrolyte.[8] **Cl$_2$Sn$^{IV}$PEGP** was prepared by refluxing PEGylated porphyrin ligand with excess amount (10 equiv.) of $SnCl_2 \bullet 2H_2O$ in anhydrous pyridine for 3 h. Treating the reaction mixture with citric acid, followed by the extraction in $CH_2Cl_2$ yielded the crude product, which was purified using the column chromatography. The yield of **Cl$_2$Sn$^{IV}$PEGP** was 81% and the purity of the final product was confirmed using typical spectroscopy techniques, such as NMR, UV-visible, and ESI-MS.

**Cl$_2$Sn$^{IV}$PEGP** exhibited a high catalytic current density (4.6 mA/cm$^2$) with an FE of 94% for $H_2$ production.[8] The TOF was 1099 s$^{-1}$ in the presence of 16 mM TFA as the proton source. Spectroelectrochemical analysis and density functional theory (DFT) calculations revealed that this Sn–porphyrin catalyst followed an

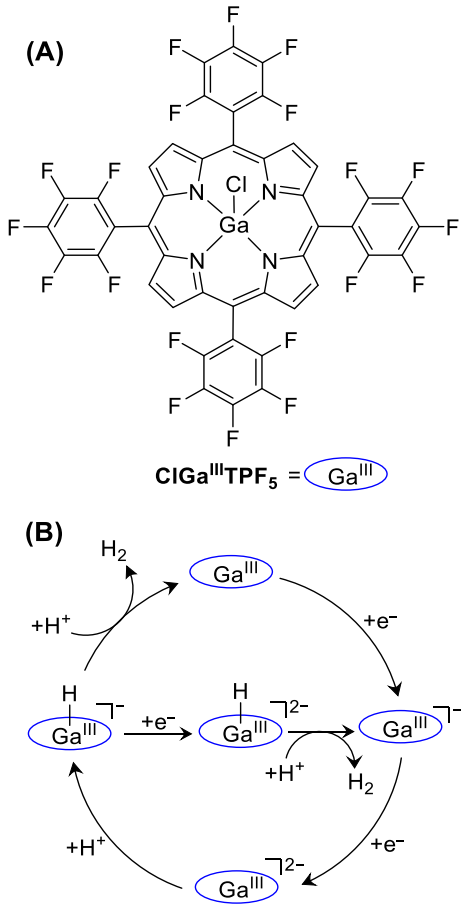


**Fig. 2.** (A) Ga(III) chloride tetrakis(pentafluorophenyl)porphyrin studied for electrochemical HER and (B) its mechanism for producing $H_2$ via a Ga–hydride intermediate. Adapted with the permission of Ref. 20.

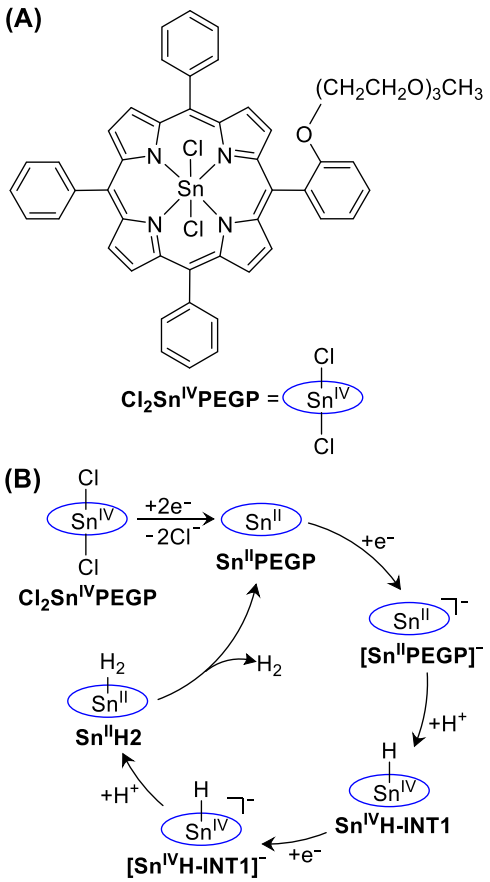


**Fig. 3.** (A) Sn porphyrin and (B) its electrochemical mechanism for the HER in a non-aqueous electrolyte. Adapted with the permission of Ref. 8.

ECEC pathway for the HER, where E and C denote $e^-$ and $H^+$ transfer events, respectively. Cyclic voltammetry data also supported the HER mechanism. In brief, a reductive wave at –0.8 V with a small (~0.01 mA) peak current was observed upon adding TFA in the bulk electrolyte solution. The peak potential of such a cathodic wave started to shift toward more positive potentials as the TFA concentration was increased, suggesting the protonation step at the Sn center. Furthermore, the "peak-shift" analysis with the logarithm of TFA concentration revealed a Nernstian EC step at the beginning of the electrochemical mechanism, also in good agreement with the DFT data. In brief, **$Cl_2Sn^{IV}$PEGP** was first reduced by $2e^-$ to form **$Sn^{II}$PEGP**, which proceeded via the ECEC mechanism to generate the Sn(IV)PEGP–hydride species, **$Sn^{IV}$H–INT1** (Fig. 3B). We confirmed the generation of **$Sn^{IV}$H–INT1** by reporting an $^1$H NMR signal at –0.9 ppm, which is attributed to the Sn(IV)–H species. Moreover, we proposed that **$Sn^{IV}$H–INT1** was further reduced by $1e^-$ to **[$Sn^{IV}$H–INT1]$^-$**. The second protonation of **[$Sn^{IV}$H–INT1]$^-$** generated an Sn(II)–PEGP–$H_2$ intermediate (**$Sn^{II}H_2$**), which released $H_2$ as the product. Overall, this is a novel example of an Sn-based molecular electrocatalyst that generates $H_2$ in a non-aqueous medium.

In addition to our reported molecular Sn(IV) electrocatalyst, Sn-doped $MoS_2$ electrodes have been studied for their electrochemical HER activity.[21] A previous study reported a synthesized multilayered $MoS_2$ with Sn dopants, and spectroscopic methods were employed to characterize the materials. These materials performed the HER over 12 h at a current density of 10 mA/cm$^2$ in an aqueous electrolyte.

**Sb:** Sb macrocycles, such as Sb porphyrin[22] and Sb salen[7] complexes, have been studied for their electrochemical HER activities. Brudvig et al. investigated a series of Sb(V) porphyrins and determined that a 5,10,15,20-tetra(*p*-tolyl)porphyrin ligand chelating with an Sb(V) center (**TPSb(OH)$_2$**, Fig. 4A) is a promising molecular HER electrocatalyst in a non-aqueous electrolyte.[22] Notably, both the porphyrin ligand and Sb metal center were redox active during the electrocatalytic HER, which is rarely observed for Sb-based catalysis. Furthermore, bulk electrolysis performed over 2 h using **TPSb(OH)$_2$** showed a stable catalytic current owing to the HER, with an FE of 62% for $H_2$. Mechanistic insights into the HER catalyzed by **TPSb(OH)$_2$** were also obtained using DFT calculations. Two consecutive ligand-centered reductions coupled with a single $H^+$ transfer eliminated one molecule of water and generated a Sb(III) porphyrin derivative (**TPSb$^{III}$**, Fig. 4B). These **TPSb$^{III}$** species then underwent a CEC pathway, where C and E denote $H^+$ and $e^-$ transfers, respectively, to generate the **TPSbH$_2$** species via two consecutive intermediates, **TPSbH–INT1** and **TPSbH–INT2**. Finally, **TPSbH$_2$** released $H_2$ and returned to **TPSb$^{III}$** via the intermediate **TPSb$^{IV}$**. The free energy change ($\Delta G$) associated with the step from **TPSbH–INT2** to **TPSbH$_2$** was 3.2 kcal/mol, with a $\Delta G$ activation at 16.2 kcal/mol. Furthermore, the H–H bond length in **TPSbH$_2$** was 0.76 Å, which is similar to that in an isolated $H_2$ molecule. Additionally, the distance between Sb and $H_2$ in the **TPSbH$_2$** intermediate was 3.3 Å, indicating a weak interaction that could ease the release of $H_2$ as the final product.

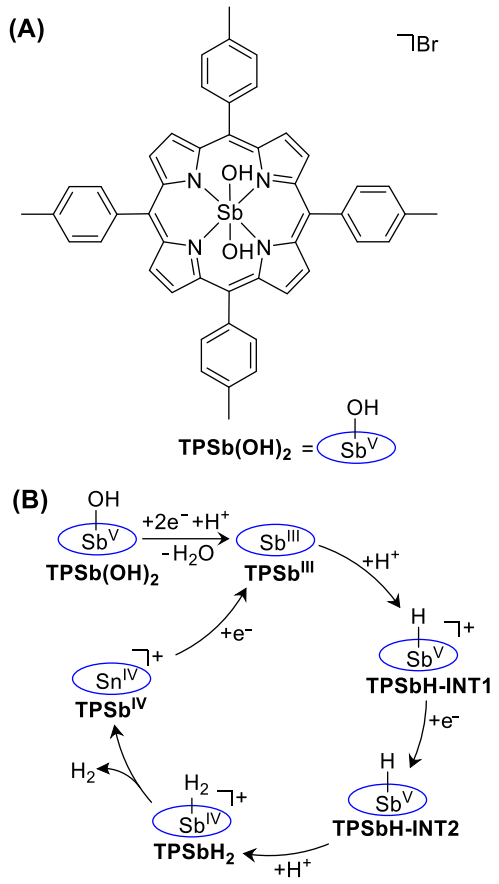


**Fig. 4.** (A) Sb(V) porphyrin, TPSb(OH)$_2$, and (B) its mechanism for electrochemical HER in a non-aqueous electrolyte. Adapted with the permission of Ref. 22.

Motivated by the activity of **TPSb(OH)$_2$** in the electrochemical HER, we recently developed a Sb(III) salen complex (**SbSalen**, Fig. 5) and reported its activity toward the electrochemical HER by immobilizing it onto C-paper working electrodes.[7] **SbSalen** complex was synthesized by stirring 2.5 equiv. of triethylamine and 1 equiv. of salen ligand in dry $CH_2Cl_2$ for 25 mins, followed by the addition of $SbCl_3$ (1 equiv.) at 0 °C under the $O_2$-free condition. Further stirring

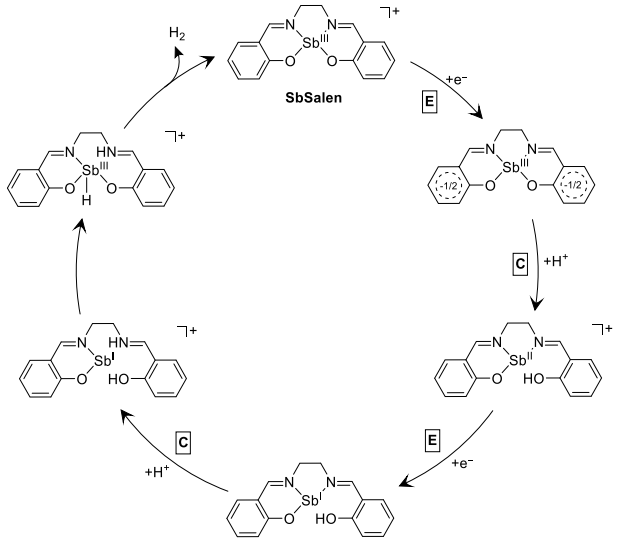


**Fig. 5. SbSalen** complex and its promoted ECEC mechanism for the HER. Adapted with the permission of Ref. 7.

for 24 h yielded a yellow suspension which was filtered and thoroughly washed with $CH_2Cl_2$ and hexane to obtain pure **SbSalen** in ~70% yield.

In an aqueous medium, we observed a high catalytic current of 30 mA/cm$^2$, with a TOF of 43.4 s$^{-1}$ using **SbSalen**. Furthermore, DFT calculations revealed that the electrochemical HER mechanism was promoted by the **SbSalen** complex, which underwent the ECEC pathway (Fig. 5). Notably, the protonation of **SbSalen** for these C steps occurred at the O or N atom of the salen ligand, not at the Sb center. Moreover, once both the O and N atoms were protonated at the end of the ECEC steps, the H atom attached to the O atom was transferred to the Sb center and formed an Sb(III)–hydride species. Our computational calculations supported this H-atom transfer from the O atom to the Sb center, because the kinetic barrier of bond dissociation was less for the O–H bond (0.28 eV) than that for the N–H bond (0.49 eV). However, these Sb(III)–hydride species released molecular $H_2$ as a product and returned to the resting state of the

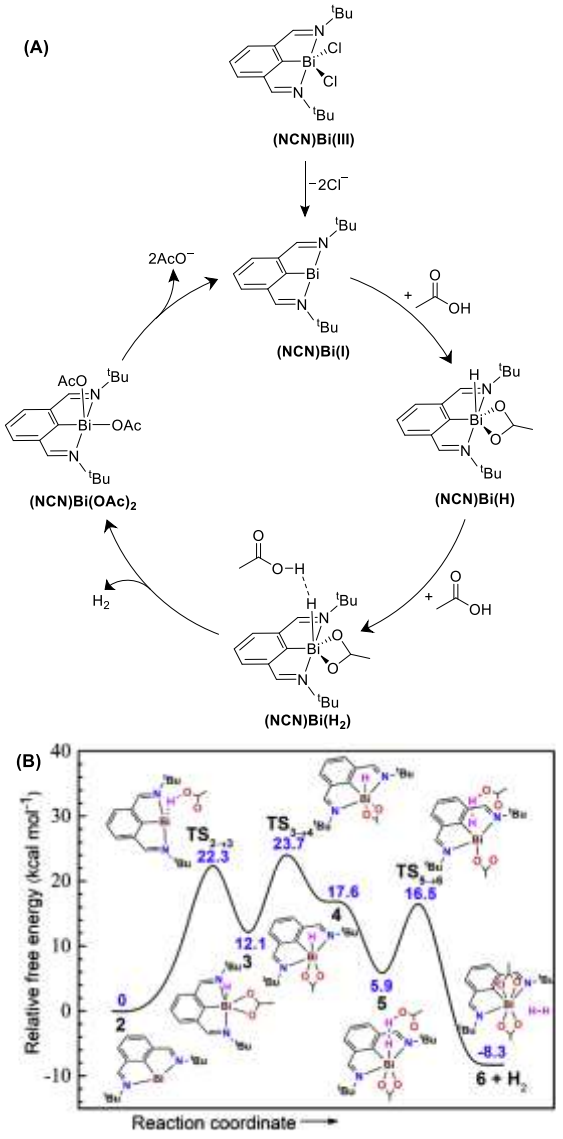


**Fig. 6.** (A) Molecular Bi(III) HER electrocatalyst and (B) energy profile for its promoted HER pathway. Adapted with the permission of Ref. 23.

**SbSalen**. Moreover, **SbSalen** produced $H_2$ with 100% FE in an aqueous medium, which is a unique example of an Sb electrocatalyst for the HER. The stability of **SbSalen** immobilized onto the C-paper was tested over 3 h, and further studied using X-ray photoelectron spectroscopy (XPS). The XPS data revealed that no demetallation event occurred during the electrolysis. Additionally, no change in the oxidation state of Sb was observed upon the completion of the catalysis, indicating the overall molecular integrity of the catalyst throughout the electrochemical HER process.

**Bi:** Bi as the active center of Bi-based molecular HER electrocatalysts is rare, except for an example reported by Luo et al.[23] They successfully synthesized a Bi complex that chelated with an NCN-type pincer ligand (**(NCN)Bi(III)**, Fig. 6A) for proton reduction under weakly acidic conditions.[23] This study reported that the HER mechanism involved the generation of a low-valent Bi(I) complex (**(NCN)Bi(I)**) that was reactive toward weak acids (Fig. 6A). At the beginning of the Bi-catalyzed HER in the presence of AcOH, **(NCN)Bi(III)** was reduced by 2e$^-$ to form **(NCN)Bi(I)**, which formed a six-coordinated Bi–hydride species that chelated with AcOH, **(NCN)Bi(H)**. These Bi–hydrido species underwent a series of configuration changes before interacting with the second molecule of AcOH (Fig. 6B). The coordination of the second AcOH molecule protonated the Bi–hydrido species and generated $H_2$ molecules via the intermediate **(NCN)Bi(H$_2$)**. Finally, the intermediate **(NCN)Bi(OAc)$_2$** was formed and returned to the **(NCN)Bi(I)** complex to complete the cycle. A detailed investigation of the DFT calculations determined the transition state structures and energy profiles (Fig. 6B), where the release of $H_2$ at the final stage of the catalytic cycle was thermodynamically favorable.

The performance of the main-group-based electrocatalysts toward HER such as turnover frequency, overpotential, and Faradaic efficiency have been tabulated in Table 1 and also shown in Figs.7A-7C. Besides molecular electrocatalysts, inorganic materials comprising the transition metal and main-group elements, especially phosphides have been explored for the production of $H_2$.[24,25] Noteworthy, the electrocatalytic HER promoted by $Ni_xP_y$ materials was impressive as their performance was comparable to the most efficient Pt-based materials. The morphologies of such inorganic materials containing various transition metals and phosphides are shown in Fig. 7D.[24]

**Table 1.** Comparative electrochemical performance of main-group-based molecular HER electrocatalysts.

| Catalyst | Solvent | Turnover frequency ($s^{-1}$) | Overpotential (V) | Faradaic efficiency (%) |
|---|---|---|---|---|
| Al-BIP | THF | $1.1\times10^{-4}$ | 0.54 | 85 |
| $ClGaTPF_5$ | MeCN | $9.4\times10^{4}$ | ~1.0 | 97 |
| $Cl_2SnPEGP$ | MeCN | $1.1\times10^{3}$ | 0.9 | 94 |
| $TPSb(OH)_2$ | MeCN | $1.2\times10^{-3}$ | 0.6 | 62 |
| SbSalen[a] | $H_2O$ | 43.4 | 1.4 | ~100 |
| (NCN)Bi(III) | MeCN | $\sim1.8\times10^{3}$ | 0.69 | 88 |

[a]*immobilized onto carbon paper electrodes*

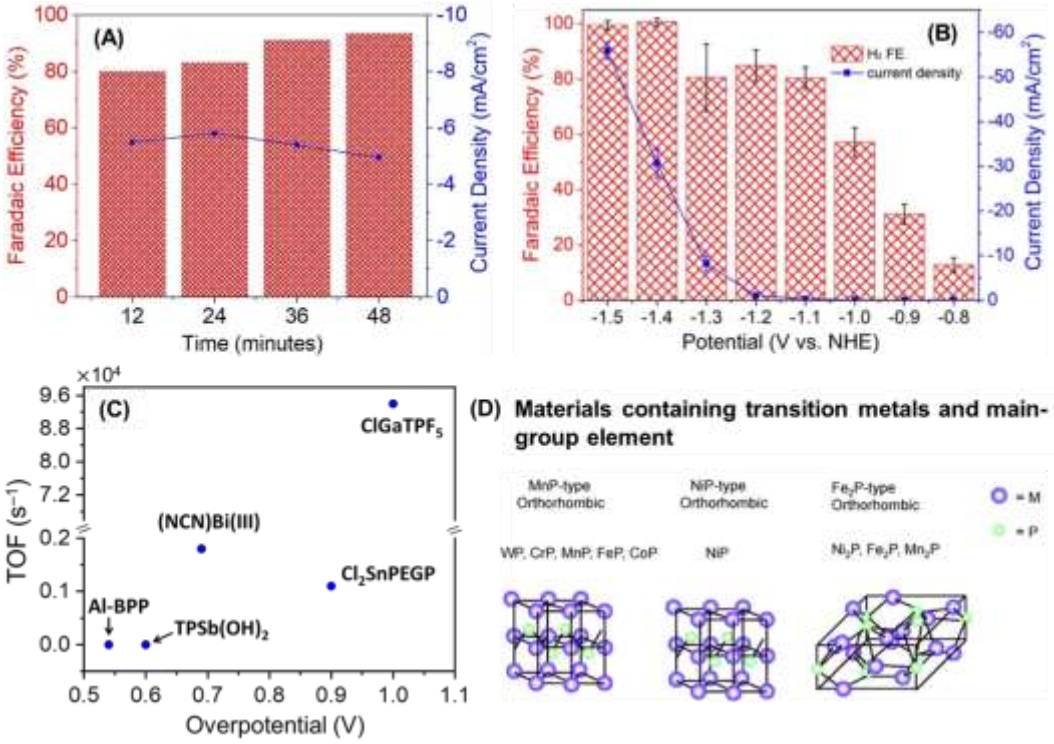


**Fig. 7.** Faradaic efficiencies and current densities observed for (A) **$Cl_2SnPEGP$** under homogeneous and (B) **SbSalen** under heterogeneous conditions for the electrochemical HER. Adapted with the permission of Refs. 8 and 7. (C) Benchmarking the maximum turnover frequencies and overpotentials for reported molecular HER electrocatalysts, **Al-BPP**, **$TPSb(OH)_2$**, **(NCN)Bi(III)**, **$Cl_2SnPEGP$**, and **$ClGaTPF_5$**. (D) Inorganic materials containing transition metals and phosphide for efficient electrochemical HER. Adapted and slightly modified with the permission of Ref. 24.

**Main group element assisted HER**

Main-group elements often assist in the electrochemical HER rather than acting as active sites of the catalysts. In particular, the presence of main-group elements enhances HER kinetics by acting as co-catalysts. In this section, we briefly highlight examples and discuss roles of the main-group elements in the HER.

**Ge:** Ge can be used as an electrode in the HER and forms Ge hydroxide (Ge–OH) functionalities when the electrodes are anodically polarized. In 1960, Gerischer et al. proposed that Ge–OH electrodes can react with $1H^+$ and $1e^-$ to generate Ge radicals on the surface, with $H_2O$ as a product.[26] The Ge radicals formed Ge hydride (Ge–H) in the presence of $H^+$, and a further reduction with $1H^+$ and $1e^-$ produced $H_2$. Memming and Neumann supported Ge electrode-promoted HER mechanisms using cyclic voltammetry (CV) data.[27] They further determined that the formation of Ge radicals and Ge–H species on the electrode surface was potential-dependent and could be controlled by tuning the potential window while cathodically scanning. In addition, they reported that the number of electrons in the conduction band at the electrode surface determined the electron-transfer kinetics, which could be enhanced by applying more negative potentials to the cathode.

**Bi:** The effects of Bi on Pb electrodes were investigated for HER in an $H_2SO_4$ solution.[28] Less than 0.733 wt% Bi was added to the commercially purchased Pb to generate the Bi–Pb alloys, which were deposited onto the pure Pb electrodes. By varying the Bi content, the authors demonstrated that the HER rate depended on the Bi loading; thus, a higher Bi content resulted in higher HER kinetics.

**Main group element assisted $CO_2$RR**

The main-group elements that serve as the active sites of molecular electrocatalysts for $CO_2$RR are not yet known. The effects of the main-group elements in assisting the $CO_2$RR, either as promoters or dopants, have been well explored. In particular, metals in Groups 1 and 2 are effective in enhancing the reaction kinetics, product selectivity, and thermodynamic stabilization of the rate-determining step during the electrochemical $CO_2$RR. In this section, we focus on the main-group elements that support the $CO_2$RR as co-catalysts.

**Li, Na, K, Rb, and Cs:** Monovalent cations of alkali metals ($M1^+$), such as $Li^+$, $Na^+$, $K^+$, $Rb^+$, and $Cs^+$, typically participate as Lewis acids in the homogeneous electrochemical $CO_2$RR. A brief discussion of the stepwise $CO_2$ activation mechanism highlights the key effects of alkali metal cations on electrochemical $CO_2$ reduction chemistry. Herein, we consider the example of a chloro–iron(III) –tetraphenylporphyrin (**$ClFe^{III}TPP$**, Fig. 8A)-electrocatalyzed $CO_2$RR in the presence of $Li^+$ or $Na^+$.[2] The electrochemical data supported that adding $Li^+$ or $Na^+$ to a $CO_2$-saturated non-aqueous electrolyte enhanced the catalytic current in the presence of **$[Fe^{III}TPP]^+$**. The stepwise mechanism of the $CO_2$RR (Fig. 8B) indicated that **$ClFe^{III}TPP$** first underwent three sequential $1e^-$ reduction events to generate the **$[Fe^{0}TPP]^{2-}$** species, which attached to $CO_2$ and formed a **$[Fe^{II}TPP–CO_2]^{2-}$** adduct. In the presence of an alkyl metal ion ($M1^+$, such as $Li^+$ or $Na^+$), the O atom of the **$[Fe^{II}TPP–CO_2]^{2-}$** adduct joined with $M1^+$ to form the

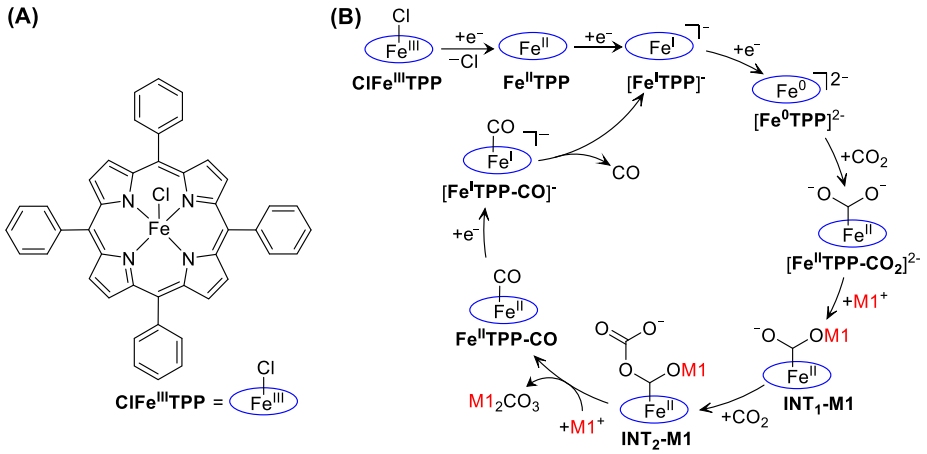


**Fig. 8.** (A) Structure of **ClFe$^{III}$TPP** for the electrochemical $CO_2$ reduction. (B) M1$^{+}$-assisted electrochemical $CO_2$-to-CO conversion. Adapted with the permission of Ref. 2.

intermediate **INT$_1$–M1**, followed by the binding of a second molecule of $CO_2$ to yield the intermediate **INT$_2$–M1** (Fig. 8B). The addition of another M1$^{+}$ to such an intermediate can produce a Li or Na carbonate salt, **M1$_2$CO$_3$**, as well as **Fe$^{II}$TPP–CO**. To complete the catalytic cycle, **Fe$^{II}$TPP–CO** was further reduced to regenerate [**Fe$^{I}$TPP**]$^{-}$ upon the formation of CO as the $CO_2$-reduced product. However, the primary role of M1$^{+}$ was to provide electrophilic assistance upon ion pairing with the [**Fe$^{II}$TPP–CO$_2$**]$^{2-}$ adduct to break (or weaken) the C–O bond of $CO_2$. Stronger Lewis acids were better at weakening the C–O bond in the [catalyst–$CO_2$] adduct, and higher turnover numbers were observed in the presence of Li$^{+}$ compared to that of the Na$^{+}$ ions. Overall, two moles of M1$^{+}$ were required to selectively reduce one mole of $CO_2$ to one mole of CO.

**Effect of alkali metals in the rate-determining step of $CO_2$RR:** Notably, the overall rates of $CO_2$RR using M1$^{+}$ ions were comparable to those measured for the same reaction using weak Brønsted acids, such as 1-propanol, 2,2,2-trifluoroethanol, and 2-pyrrolidone.[3,4] Furthermore, alkali metal ions could boost the rate of the $CO_2$ insertion into a transition metal–hydride bond during $CO_2$RR.[29] For example, the rate of $CO_2$ insertion into a Ru–hydride bond in a Ru complex bearing 2,2'-bipyridine and 2,2':6',2"-terpyridine chelating ligands was measured in the presence of Li$^{+}$, Na$^{+}$, K$^{+}$, or Rb$^{+}$, and the rate enhancement trend for the $CO_2$ insertion reaction was as follows: Li$^{+}$ >> Na$^{+}$ > K$^{+}$ > Rb$^{+}$ (Table 2).[29] These observations suggested that monovalent alkali metal ions with smaller sizes have more Lewis acidic character and thus, provide more stabilization to the rate-determining transition state during $CO_2$RR.

**Role of alkali metals in $CO_2$RR selectivity:** Alkali metal cations are often crucial for determining product selectivity in $CO_2$RR. For example, the $CO_2$RR performed using polycrystalline Au, Cu, and Ag electrodes in a pure sulfuric acid ($H_2SO_4$) electrolyte showed no CO production (primary C1 product in $CO_2$RR) without alkali metal cations.[30] This poor $CO_2$RR selectivity in the absence of alkali metal cations is likely due to the desolvated alkali metal cations building an electrostatic interaction with an O atom (or both O atoms) of the $CO_2^{-}$ intermediate after the [catalyst–$CO_2$] adduct formed. If these electrostatic interactions were not established during the $CO_2$RR, the selectivity toward CO formation would be poor. A model DFT calculation studied for the Au-electrode catalyzed $CO_2$RR in the presence of an alkali cation suggested that such electrostatic interactions could lower the Gibbs free energy of $CO_2$ adsorption (by at least 0.5 eV) at the electrode surface.[30] Additionally, the O–C–O bond angle decreased from 180° (linear) to below 140° (bent) when the [catalyst–$CO_2$] adduct was electrostatically stabilized by the alkali metal cations.[30] This change in $CO_2$ geometry during the $CO_2$RR often favors faster electron transfer from the electrode surface to $CO_2$, which was observed using the Cs$^{+}$ ion with Au electrodes.[30,31] Furthermore, the electrostatic interactions of metal cations and electrode surfaces could enhance the electric field at the interface of the electrode surface and bulk electrolyte, and the enhanced electric field could influence the adsorption of the $CO_2^{-}$ species at the electrode surface.[32–34] Consequently, higher adsorption of $CO_2^{-}$ at the electrodes, as well as subsequent proton-transfer events, could result in better product selectivity for $CO_2$RR.[35]

**Table 2.** Rate of $CO_2$ insertion reaction into an Ru–hydride bond of an Ru diimine complex in the presence of Li$^{+}$, Na$^{+}$, K$^{+}$, or Rb$^{+}$ in acetonitrile. Adapted with permission from Ref. 29.

| Additive | Rate constant ($M^{-2}\cdot s^{-1}$) |
|---|---|
| $LiNTF_2$[a] | 3.1 |
| LiOTf[b] | 3.0 |
| $LiBPh_4$[c] | 3.0 |
| $NaBAr^F{}_4$[d] | 0.40 |
| NaOTf | 0.40 |
| $NaBPh_4$ | 0.37 |
| $NaNTF_2$ | 0.34 |
| $KPF_6$ | 0.25 |
| $KBPh_4$ | 0.21 |
| $KNTf_2$ | 0.20 |
| $RbBPh_4$ | 0.01 |

[a]$NTf_2$ = bis(trifluoromethane)sulfonamide; [b]OTf = trifluoromethanesulfonate; [c]$BPh_4$ = tetraphenylborate; [d]$BAr^F{}_4$ = tetrakis[3,5-bis(trifluoromethyl)phenyl]borate. Note: All rate constants are reported at room temperature.

**Role of alkali metals in $CO_2$RR kinetics:** The rate of product formation relies on the nature of the monovalent cations, which is defined by the Lewis acidity of the alkali metal ions and their hydration number.[36,37] This hypothesis is supported by several reports, in that weakly hydrated $Cs^+$ and $K^+$ afforded high current densities during electrochemical $CO_2$RR in the aqueous electrolytes, regardless of the pH.[34,37,38] Electrochemical $CO_2$RR using gas diffusing electrodes further supported that high partial current densities for CO production were observed in the presence of alkali metal cations in the order of $Cs^+ > K^+ > Na^+ > Li^+$.[39–42] However, the concentration of these alkali metal solutions should be low enough, <1.0 M, to avoid the background bicarbonate reduction promoted by the cations.[43]

**Mg, Ca, and Ba:** The Lewis acidities of alkaline-earth metals can influence the electrochemical $CO_2$RR, similar to the abovementioned discussion for alkali metals; however, they follow different $CO_2$RR pathways than that for the alkali metal-assisted $CO_2$RR. The dicationic forms of three alkaline earth metals ($M2^{2+}$), $Mg^{2+}$, $Ca^{2+}$, and $Ba^{2+}$, are known to enhance $CO_2$RR rates.[2] Herein, we focus on the stabilization strategies of the [catalyst–$CO_2$] adduct in the presence of $M2^{2+}$ ions and how such strategies differ from those observed in $M1^+$-supported [catalyst–$CO_2$] adduct stabilization. For further discussion, we chose the example of the **ClFe$^{III}$TPP**-catalyzed $CO_2$RR and examined the effects of $M2^{2+}$ ions on the stabilization of the **[Fe$^{II}$TPP–$CO_2$]$^{2-}$** adduct during the $CO_2$RR (Fig. 9). As shown in Fig. 8B, stabilization of the **[Fe$^{II}$TPP–$CO_2$]$^{2-}$** adduct is crucial for the $CO_2$RR. Therefore, we discuss two different strategies followed by the $M2^{2+}$ ions (paths A and B in Fig. 9) to stabilize the **[Fe$^{II}$TPP–$CO_2$]$^{2-}$** adduct. Following path A, a single $M2^{2+}$ ion could interact with both O atoms of **[Fe$^{II}$TPP–$CO_2$]$^{2-}$** electrostatically, forming the intermediate **INT1–M2**. Eventually, the second molecule of $CO_2$ reacted with **INT1–M2** to produce metal carbonate salts ($M2CO_3$) and CO products. In contrast, if $M2^{2+}$ interacted with only one O atom of **[Fe$^{II}$TPP–$CO_2$]$^{2-}$** following path B (Fig. 9), an **INT2–M2** intermediate was formed. **INT2–M2** was then reduced using a weak Brønsted acid to generate formate ($HCO_2^-$) as the final $CO_2$-reduced product. A mixture of products was often obtained from the $CO_2$RR in the presence of $M2^{2+}$ ions. For example, 70% CO and 30% $HCO_2^-$ were obtained via the $CO_2$RR using **[Fe$^{III}$TPP]$^+$** in the presence of $Mg^{2+}$. Furthermore, these experiments were repeated using two different $M2^{2+}$ ions, $Ca^{2+}$ and $Ba^{2+}$, to compare the overall rate of the $CO_2$RR. A similar apparent rate constant, $1.5 \times 10^4$ $M^{-2}{\cdot}s^{-1}$, was estimated for $Mg^{2+}$ and $Ca^{2+}$, which was comparatively higher than that observed in the presence of $Ba^{2+}$ ($3.0 \times 10^3$ $M^{-2}{\cdot}s^{-1}$).[2] However, the first-order reaction in $M2^{2+}$ concentration was observed for the $CO_2$RR, indicating that only one mole of $M2^{2+}$ was sufficient to complete the $CO_2$RR cycle, whereas the order of the reaction was 2 when alkali metal ions, $M1^+$, were used. This suggests that smaller equivalents of $M2^{2+}$ ions can effectively enhance the $CO_2$RR selectivity.

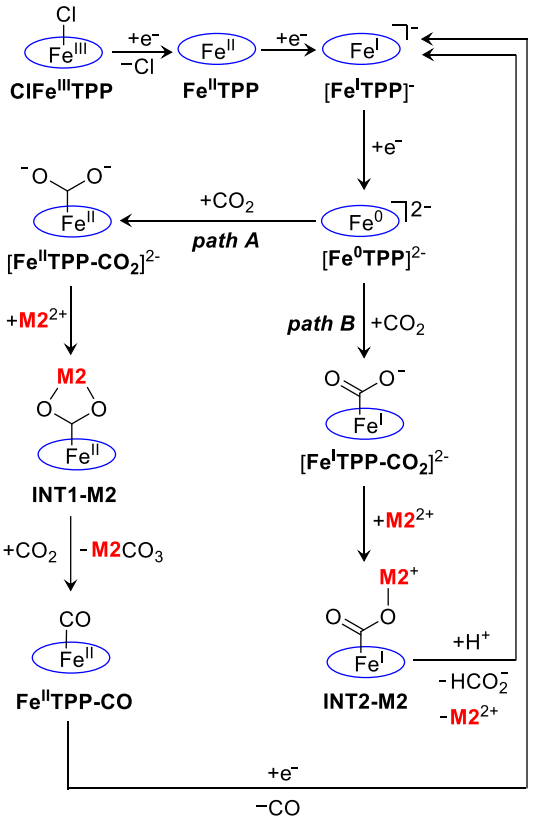


**Fig. 9.** $Mg^{2+}$, $Ca^{2+}$, or $Ba^{2+}$-assisted electrochemical $CO_2$-to-CO conversion catalyzed by **ClFe$^{III}$TPP**. Adapted with the permission of Ref. 2.

Further molecular evidence of the [catalyst–$CO_2$–$M2^{2+}$] intermediate formation in the $CO_2$RR cycle was revealed using cobalt phthalocyanine (CoPc)-modified Au electrodes in the presence of $Mg^{2+}$ (Fig. 10A).[44] CV data revealed that these CoPc-modified Au electrodes exhibited high catalytic currents with approximately 80% FE for CO formation when 0.05 M of $Mg^{2+}$ ions were present in a $CO_2$-saturated 0.1 M $KHCO_3$ electrolyte. Scanning tunneling microscopy (STM) images were captured for the CoPc monolayer on the electrode surface following $CO_2$ adsorption, and the apparent thickness of the layer was estimated to be ~0.15 nm. The thickness increased to ~0.19 nm when STM images were taken for the same in $CO_2$-saturated $Mg(ClO_4)_2$ solution,[44] indicating $Mg^{2+}$ ions were networked to the CoPc–$CO_2$ complex on the surface via electrostatic interactions. Additionally, high-resolution STM images collected after performing $CO_2$RR at –1.1 V vs. saturated calomel electrode (SCE) showed only the presence of the Co atom and phthalocyanine macrocycle, without the existence of $Mg^{2+}$, further confirming that $Mg^{2+}$ assisted in stabilizing the [CoPc–$CO_2$] adduct without getting adsorbed onto the electrode surface. Notably, when similar $CO_2$RR processes were performed using CoPc-modified Au electrodes in different alkaline-earth metal electrolytes, such as $Ca(ClO_4)_2$ and $Ba(ClO_4)_2$, the apparent layer height of the CoPc monolayer was similar to that observed in the $CO_2$- and $M2^{2+}$-free solutions after saturation with $CO_2$. These data further highlight that $Mg^{2+}$ ions play a unique role in supporting $CO_2$ binding at the active center of the

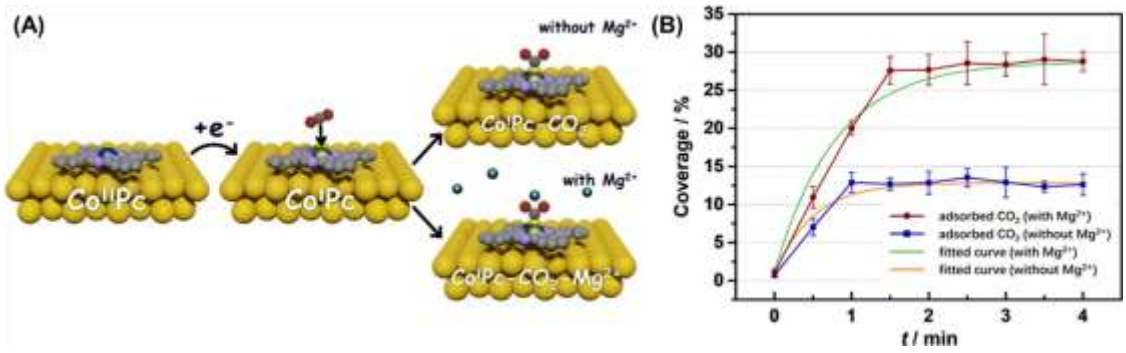


**Fig. 10.** (A) CoPc-modified Au electrodes, and the proposed steps to form CoPc–$CO_2$ and CoPc–$CO_2$–$Mg^{2+}$ complexes. (B) Surface coverage estimated based on *in situ* electrochemical STM and simulated data for $CO_2$ binding with and without $Mg^{2+}$ ions. Adapted with the permission of Ref. 44.

catalyst. To gain more insight into the effect of $Mg^{2+}$ on $CO_2$ adsorption and binding to the catalytic center, *in situ* electrochemical STM (ECSTM) was performed for an identical CoPc-modified electrode, and the surface coverage of the adsorbed $CO_2$ onto the catalyst-immobilized electrode was estimated. In the $CO_2$-saturated $Mg(ClO_4)_2$ electrolyte, the average surface coverage was approximately 30% (Fig. 10B), which was much lower when the electrolyte was changed to $NaClO_4$ (12.6%), $Ca(ClO_4)_2$ (17%), or $Ba(ClO_4)_2$ (14.4%). Furthermore, the rate constant of $CO_2$ adsorption in the $Mg(ClO_4)_2$ solution was 0.36 $min^{-1}$, which was higher than that in the $Mg^{2+}$-free solution (0.26 $min^{-1}$). In contrast, the rate of $CO_2$ desorption from the surface was 0.89 $min^{-1}$ in the presence of $Mg^{2+}$, compared with 1.77 $min^{-1}$ in the $Mg^{2+}$-free electrolyte. Additional calculations of the $\Delta G$ for the formation of CoPc–$CO_2$ and CoPc–$CO_2$–$Mg^{2+}$ complexes indicated that CoPc–$CO_2$–$Mg^{2+}$ ($\Delta G$ = –0.142 eV) was more thermodynamically stable than the CoPc–$CO_2$ complex ($\Delta G$ = –0.038 eV). Together, these results indicate that $Mg^{2+}$ acts as an efficient stabilizer to increase the $CO_2$ adsorption/binding rate at the catalyst active site(s), thereby influencing the overall $CO_2$RR kinetics.

**B:** B-centered catalysts are not commonly used for $CO_2$RR catalysis, except in a few reports in which B acts as a dopant. One example is a B-doped diamond electrode (BDDE), which alters the electrochemical $CO_2$RR pathway by avoiding the typical generation of $CO_2^{\bullet-}$ in the elementary $CO_2$RR step.[45] In the $CO_2$RR pathway promoted by BDDEs, $CO_2$ binds to the electrode surface as monodentate carbonate, [BDDE–O–$CO_2^{2-}$] (Fig. 11), instead of forming the [BDDE–$CO_2$] adduct in the $CO_2$-saturated aqueous electrolyte. *In situ* attenuated total reflectance infrared (ATR-IR) spectroscopy confirmed the presence of the carbonate group at the BDDE surface, with strong absorption peaks at 1530–1470 and 1370–1300 $cm^{-1}$ due to the vibration of –O–$CO_2$.[45] Notably, the intensity of these ATR-IR absorption peaks increased with time as more $CO_2$ was adsorbed at the electrode surface upon saturation with $CO_2$. This $CO_2$ activation at the BDDE is termed the "self-activation" process, which increases the effective electroactive area toward $CO_2$RR.[45] Next, those carbonate moieties at the BDDE were converted to carboxylic groups following a proton-coupled electron transfer (PCET) step and finally to formate, which was released as a $CO_2$-reduced product. The electrical-to-chemical energy conversion efficiency for $CO_2$RR using the BDDE was 50% for the production of formate (or formic acid, depending on the pH of the solution) from $CO_2$. Although the actual role of immobilized B in BDDE is yet to be explored, B-doped electrodes could be promising for generating formate from $CO_2$ via selective carbonate intermediates.

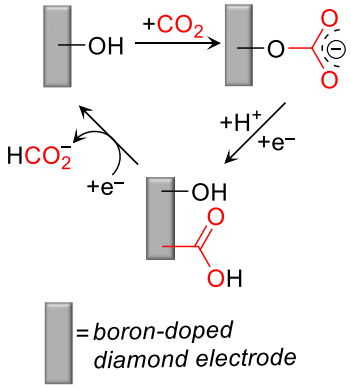


**Fig. 11.** Proposed steps for the electrochemical $CO_2$RR using B-doped diamond electrodes (BDDEs). Adapted with the permission of Ref. 45.

Another example of a B-supported electrochemical $CO_2$RR was reported by Liu et al., in which they introduced B into a single atomic Fe site complex.[46] Using a B-incorporated single atomic Fe electrocatalyst, ~99% FE for CO production with a current density of 130 $mA/cm^2$ was observed in $CO_2$-saturated 0.1 M $KHCO_3$ buffer after performing bulk electrolysis in a membrane-separated H-cell. Under these electrochemical conditions, the presence of B near the Fe active site in the single-Fe-atom complex enhanced the reaction kinetics for the overall $CO_2$RR. Furthermore, the investigation of double-layered capacitance revealed that the presence of B enhanced the effective electrochemical surface area of the B-supported single Fe atom electrodes and exposed more active sites, resulting in better electrode–$CO_2$ interaction.[46] Thus, faster $CO_2$RR kinetics were obtained using the B-incorporated single Fe atom electrocatalysts.

**Ga:** CO is a common $C_1$ product in the electrochemical $CO_2$RR cycle; however, using Ga in catalysts has been primarily reported for producing more value-added products, such as methane ($CH_4$), formic acid (HCOOH), ethane ($C_2H_6$), ethylene ($C_2H_4$), *n*-propanol ($C_3H_7OH$), and methylglyoxal ($CH_3COCHO$).[47–49] In this section, we discuss these examples and the role of Ga in electrocatalytic $CO_2$RR cycles.

Sekimoto et al. demonstrated the performance of Sn- or Si-doped Ga oxide ($Ga_2O_3$) electrodes for the selective production of HCOOH with >80% FE in the electrochemical $CO_2$RR.[47] The authors revealed that the FE for HCOOH formation was independent of the type of dopant (Sn or Si) present in the $Ga_2O_3$ electrodes. Therefore, the selective $CO_2$RR toward the formation of only HCOOH could be credited to the performance of the $Ga_2O_3$ electrodes. Thermodynamic insights into HCOOH formation at the $Ga_2O_3$ electrodes were also obtained using DFT. Protonation occurred at the C center following $CO_2$ adsorption on the $Ga_2O_3$ surface, yielding the [HCOO–$Ga_2O_3$] adduct, in which the two O atoms coordinated with the Ga sites. The distance between one Ga atom and one O atom was 0.20 nm, and such weak binding could help the desorption of the product (such as HCOOH) after [HCOO–$Ga_2O_3$] was reduced by a single $H^+$ and single $e^-$. Furthermore, the $Ga_2O_3$ electrodes exhibited stable catalytic current (~0.3 mA/cm$^2$) over 50 repeating CV sweeps recorded under $CO_2$ atmosphere, indicating the robust stability of Ga electrodes for $CO_2$RR.

Lewis et al. determined that bimetallic NiGa films (NiGa, $Ni_3Ga$, and $Ni_5Ga_3$) were active electrocatalytic materials for the $CO_2$RR in a neutral bicarbonate solution.[48] Using NiGa films, $CH_4$, $C_2H_6$, and $C_2H_4$ were obtained as the primary $CO_2$-reduced products at low onset potentials, with less than –0.48 V vs. reversible hydrogen electrode (RHE).[48] Furthermore, various NiGa films catalyzed the formation of $CO_2$-reduced $C_2$ products via an intermediate CO formation step. Further reduction of the CO with selective $H^+$ and $e^-$ yielded $CH_4$ and $C_2$ products. CO could bind strongly to the Ni center,[50] but the presence of Ga in bimetallic NiGa films destabilized Ni–CO interactions, resulting in the further reduction of CO toward more reduced products, such as $CH_4$ or the multi-carbon products $C_2H_4$ and $C_2H_6$.

Other than Ga-based electrodes, single-atom Ga electrocatalysts were reported for the selective $CO_2$-to-CO conversion with FEs >90%.[51] Using these single-atom Ga catalysts, much higher current densities were obtained for the electrochemical $CO_2$RR compared to the previously discussed $Ga_2O_3$ electrodes. Based on the DFT calculations, the adsorbed $CO_2$ was protonated at the rate-determining step to form the [Ga electrode–COOH] intermediate, which finally generated CO upon further reduction. Furthermore, doping single-atom Ga electrodes with heteroatoms (e.g., P and S) significantly decreased the $\Delta G$ barriers for the rate-determining step of CO generation. The P- and S-doped, single-atom Ga electrocatalysts were flexible in geometry at the Ga center, which also supported the thermodynamic parameters of the CO formation step by reducing the activation energy of the *COOH species generated at the surface of the electrode.

**Ge and Sn:** Group 14 elements rarely serve as catalytic centers for multi-$H^+$/multi-$e^-$ transfer reactions, except for a few examples of Ge- or Sn-based solid materials. For example, Ge–S–In amorphous glass materials[52] and Sn-containing electrocatalysts[53] have been reported for the $CO_2$RR owing to their high selectivity, low overpotential, and steady catalytic stability.

**Ge:** Ge–S–In chalcogenide glass materials were prepared to perform $CO_2$RR in an aqueous electrolyte.[52] Using these Ge–S–In glass electrodes, ~15% FE for CO formation at an applied potential of –1.3 V vs. normal hydrogen electrode (NHE) was determined after performing bulk electrolysis for over 5 h. Notably, when the micron-sized particles of Ge–S–In were deposited onto the C-paper electrode, a comparatively higher catalytic current was observed in the $CO_2$-saturated aqueous electrolyte. Upon performing preparative-scale electrolysis using micron-sized Ge–S–In particles adsorbed onto the C-paper, the product in the $CO_2$RR changed to HCOOH with an FE of 26.1%. Further control electrolysis without drop-casting Ge–S–In particles on the C-paper electrodes exhibited a low FE (7.1%) for HCOOH, indicating that Ge–S–In materials are required to increase the FE for HCOOH production.

**Sn:** Publications on Sn-based electrocatalytic materials for $CO_2$RR have grown since 2014.[53] Among them, metallic Sn-based catalysts have been promising for electrochemical $CO_2$RR, owing to their high surface area that enables more interaction between the catalyst and $CO_2$.[54] The enhanced interaction reduces overpotentials, thus thermodynamically proceeding in the formation of $CO_2$-reduced intermediates, COOH* or HCOO*.[55] Furthermore, different morphologies of metallic Sn electrodes, such as rod, planar sheet, and dendritic, have been tested to optimize the size and shape of the Sn electrodes with their efficiency and product selectivity toward $CO_2$RR. Moreover, the nanorod-shaped Sn electrodes selectively generated HCOOH with an FE of 94.5% at the applied potential of –1.6 V vs. Ag/AgCl.[56] Sn-containing bimetallic electrocatalysts, such as Pd–Sn,[57] Cu–Sn,[58] and Bi–Sn,[59] have also been studied for the $CO_2$RR, where $HCO_2^-$ or HCOOH is the major product. Additionally, Cu–Sn alloys are known for selective $CO_2$-to-CO conversion in $CH_3CN$ electrolytes, as reported by Sacci et al.[60]

In addition to the Sn-based materials discussed above, Sn oxide electrodes have been extensively explored. For example, Sn oxide nanoparticles immobilized onto graphene layers promoted the $CO_2$RR at only 340 mV of overpotential with >93% FE for $HCO_2^-$ formation. These electrocatalysts were stable over 18 h. Moreover, one-dimensional Sn oxide nanomaterials exhibited elevated electrochemical $CO_2$RR performance, such as high current densities and selective product formation (commonly HCOOH formation).[61] These remarkable $CO_2$RR activities are primarily attributed to the large surface area at the catalyst site, which enhances the catalyst-substrate interaction.

**P and Bi:** Group 15 elements, primarily P and Bi, are commonly used as co-catalysts in redox reactions related to small-molecule activation. Herein, we chose examples of reports that emphasize the roles of P and Bi in influencing the thermodynamic and kinetic parameters of the $CO_2$RR.

**P:** P typically assists the transition-metal-based catalysts for $CO_2$RR.[62] For example, the presence of P near a single-Fe-atom catalyst has prompted the $CO_2$RR catalysis toward the selective formation of CO with an FE of 98% and TOF of 508.8 $h^{-1}$ at the overpotential of 0.34 V.[62] When P was near the single Fe atom, the partial current densities for CO production was enhanced, and the overpotential for the overall $CO_2$RR decreased by the Fe site stabilizing at a lower oxidation state upon the formation of *COOH and *CO intermediates. Thus, the reduced Fe site could push more

electron densities to activate $CO_2$ and enabled CO desorption at the end of the catalytic cycle, as determined by DFT calculations.[62] Furthermore, similar developments of catalytic materials by incorporating P into an N-doped, C-supported single-Fe-atom catalyst, reported by Sun et al., demonstrated that 97% FE can be obtained for CO formation at 0.32 V of overpotential while performing $CO_2$RR in the aqueous electrolyte.[63] DFT calculations were in agreement; therefore, the presence of P atoms near the Fe center can support more electron localization at the Fe center, thus stabilizing the *COOH intermediate.

Cu nanocrystal catalysts doped with P have also become efficient electrocatalysts for converting $CO_2$ into ethylene (FE, ~31%) and alcohols (~45%).[64] The catalytic current density achieved in the $CO_2$RR was high (57.2 mA/cm$^2$) compared to that for the Cu catalysts without P-doping. However, the formation of $C_{2+}$ products from $CO_2$ critically depends on the thermodynamic landscape behind C–C bond formation. Chen et al. estimated that the $\Delta G$ for C–C coupling processes was more challenging ($\Delta G$ = 0.51 eV) without P ($\Delta G$ = –0.49 eV). They further reported that the presence of P atoms near Cu atoms could influence the energy levels of the Cu 3*d*-orbitals, bringing them near the Fermi level and facilitating a stronger overlap between the 3*d*-orbitals of P-doped Cu and the reduced $CO_2$ intermediates (i.e., *COHCO). Thus, these intermediates were energetically stabilized at the surface of the P-doped Cu electrodes, lowering the overpotential of the reaction.

In addition to transition metals, the introduction of P into N-doped C catalysts (N–C) also exhibited notable effects on the electrochemical $CO_2$RR. Li et al. studied metal-free C electrodes co-doped with P and N and determined their stability over 24 h of electrolysis while reducing $CO_2$ to CO with an FE of 92%.[65] DFT calculations further supported the hypothesis that the P dopant could lower the $\Delta G$ of *COOH formation and polarize the electron densities at the active site to raise the energy level near the Fermi level. This change in the energy level significantly boosted the electron-transfer process between the active site of the catalyst and $CO_2$ (or reduced $CO_2$ intermediates).

**Bi:** B-containing electrocatalysts for $CO_2$RR are often selective for the reduction of $CO_2$ to $HCO_2^-$. Here, we focus on Bi nanomaterials and B-doped Bi electrodes for the $CO_2$RR. Fan et al. revealed that the curvature of Bi nanomaterials, such as Bi nanotubes and nanosheets, could influence the thermodynamic landscape of the $CO_2$RR and product selectivity.[66] This hypothesis was investigated using Bi nanotubes with high curvature, and the catalytic current density for $CO_2$RR was 39.4 mA/cm$^2$ with 97% selectivity toward $HCO_2^-$ production. Compared with the performance of Bi nanosheets under identical electrochemical conditions, Bi nanotubes were more effective in maintaining a high FE (>90 %) for $HCO_2^-$ formation at a fixed applied potential.

An additional example of Bi-based materials for the selective $CO_2$-to-$HCO_2^-$ conversion was reported by Liu et al.[67] They prepared B-doped Bi-based electrodes and achieved 90% FE for the $HCO_2^-$ formation reaction within a wider applied potential window between –0.6 and –1.2 V vs. RHE. The incorporation of B into Bi materials enriched the electron density of Bi and altered the adsorption energy of the $CO_2$-reduced intermediate, OCHO*. These effects influenced the kinetics of the $CO_2$RR. However, Bi materials, which are less toxic, earth-abundant, and environmentally friendly, are promising for the selective $CO_2$-to-$HCO_2^-$ conversion.

## Summary

Electrochemical HER and $CO_2$RR have gained significant attention for addressing climate change and future energy infrastructure. Electrocatalytic conversion is promising in the field of chemistry, where transition-metal catalysts are in the spotlight. Despite the remarkable progress in the development of transition-metal-based electrocatalysts, electrocatalytic materials comprising main-group elements have potential for converting $CO_2$ into value-added chemicals or producing $H_2$. This article reviewed studies that explored the main-group element-based electrocatalysts for the $CO_2$RR and HER. We discussed the activities of the main-group elements by carefully selecting elements that exhibit unique roles in enhancing the $CO_2$RR or HER kinetics, product selectivity, or assisting in the intermediate stabilization steps. First, we discussed the remarkably efficient HER activities promoted by the molecular Al- and Ga-based electrocatalysts and their mechanism for producing $H_2$, resembling the pathways of the transition-metal-catalyzed HER. Next, we highlighted the performance of Ge and Sn materials for the $CO_2$RR and HER, including one of our studies that used a molecular Sn porphyrin derivative that produces $H_2$ in a non-aqueous electrolyte. Second, we discussed the selectivity of $CO_2$-to-$HCO_2^-$ using Group 13 elements, particularly B and Ga. Additionally, we focused on the Lewis acidity of the elements in Groups 1 and 2 toward $CO_2$RR selectivity and kinetics. Finally, we discussed the various roles of P, Sb, and Bi in $CO_2$RR and HER electrocatalysis under both homogeneous and heterogeneous conditions. Together, the exclusive discussion on the main-group element-promoted $CO_2$RR and HER could serve as excellent resources for progressing main-group element-based electrocatalyst design, development, and implementation in fuel-forming reactions or storing energies in chemical bonds.

## Conflicts of interest

There are no conflicts to declare.

## Acknowledgements

This study was supported by the National Science Foundation (grant no. CHE-2041436).

## References

1 P. P. Power, *Nature*, 2010, **463**, 171–177.
2 I. Bhugun, D. Lexa and J.-M. Savéant, *J. Phys. Chem.*, 1996, **100**, 19981–19985.

3 I. Bhugun, D. Lexa and J.-M. Savéant, *J. Am. Chem. Soc.*, 1996, **118**, 1769–1776.
4 I. Bhugun, D. Lexa and J.-M. Savéant, *J. Am. Chem. Soc.*, 1994, **116**, 5015–5016.
5 S. Sinha, M. S. Aaron, J. Blagojevic and J. J. Warren, *Chem. Eur. J.*, 2015, **21**, 18072–18075.
6 M. N. Jackson and Y. Surendranath, *Acc. Chem. Res.*, 2019, **52**, 3432–3441.
7 C. K. Williams, G. A. McCarver, A. Chaturvedi, S. Sinha, M. Ang, K. D. Vogiatzis and J. Jiang, *Chem. Eur. J.,* 2022*,* **28***,* e202201323.
8 A. Chaturvedi, G. A. McCarver, S. Sinha, E. G. Hix, K. D. Vogiatzis and J. Jiang, *Angew. Chem. Int. Ed.*, 2022, **61**, e202206325.
9 S. Sinha, C. K. Williams and J. Jiang, *iScience*, 2022, **25**, 103628.
10 S. Amanullah, P. Saha, A. Nayek, M. E. Ahmed and A. Dey, *Chem. Soc. Rev.*, 2021, **50**, 3755–3823.
11 N. S. Lewis and D. G. Nocera, *Proc. Natl. Acad. Sci.*, 2006, **103**, 15729–15735.
12 G. Ménard and D. W. Stephan, *J. Am. Chem. Soc.*, 2010, **132**, 1796–1797.
13 A. E. Ashley and D. O'Hare, in *Frustrated Lewis Pairs II*, eds. G. Erker and D. W. Stephan, Springer Berlin Heidelberg, Berlin, Heidelberg, 2012, vol. 334, pp. 191–217.
14 B. L. Thompson and Z. M. Heiden, *Tetrahedron*, 2019, **75**, 2099–2105.
15 E. J. Thompson and L. A. Berben, *Angew. Chem. Int. Ed.*, 2015, **54**, 11642–11646.
16 T. J. Sherbow, J. C. Fettinger and L. A. Berben, *Inorg. Chem.*, 2017, **56**, 8651–8660.
17 J. L. Dempsey, B. S. Brunschwig, J. R. Winkler and H. B. Gray, *Acc. Chem. Res.*, 2009, **42**, 1995–2004.
18 M. L. Helm, M. P. Stewart, R. M. Bullock, M. R. DuBois and D. L. DuBois, *Science*, 2011, **333**, 863–866.
19 S. Sinha, G. N. Tran, H. Na and L. M. Mirica, *Chem. Commun.*, 2022, **58**, 1143–1146.
20 N. Wang, H. Lei, Z. Zhang, J. Li, W. Zhang and R. Cao, *Chem. Sci.*, 2019, **10**, 2308–2314.
21 J. Radhakrishnan, A. Kareem, S. Senthilkumar and K. Biswas, *J. Alloys Compd.*, 2022, **917**, 165444.
22 J. Jiang, K. L. Materna, S. Hedström, K. R. Yang, R. H. Crabtree, V. S. Batista and G. W. Brudvig, *Angew. Chem. Int. Ed.*, 2017, **56**, 9111–9115.
23 W.-C. Xiao, Y.-W. Tao and G.-G. Luo, *Int. J. Hydrog. Energy*, 2020, **45**, 8177–8185.
24 P. Liu, J. A. Rodriguez, T. Asakura, J. Gomes and K. Nakamura, *J. Phys. Chem. B*, 2005, **109**, 4575–4583.
25 S. T. Oyama, T. Gott, H. Zhao and Y.-K. Lee, *Catal. Today*, 2009, **143**, 94–107.
26 H. Gerischer, A. Mauerer and W. Mindt, *Surf. Sci.*, 1966, **4**, 431–439.
27 R. Memming and G. Neumann, *J. Electroanal. Chem. Interfacial Electrochem.*, 1969, **21**, 295–305.
28 Y. M. Wu, W. S. Li, X. M. Long, F. H. Wu, H. Y. Chen, J. H. Yan and C. R. Zhang, *J. Power Sources*, 2005, **144**, 338–345.
29 J. E. Heimann, W. H. Bernskoetter and N. Hazari, *J. Am. Chem. Soc.*, 2019, **141**, 10520–10529.
30 G. Marcandalli, M. C. O. Monteiro, A. Goyal and M. T. M. Koper, *Acc. Chem. Res.*, 2022, **55**, 1900–1911.
31 B. Huang, K. H. Myint, Y. Wang, Y. Zhang, R. R. Rao, J. Sun, S. Muy, Y. Katayama, J. Corchado Garcia, D. Fraggedakis, J. C. Grossman, M. Z. Bazant, K. Xu, A. P. Willard and Y. Shao-Horn, *J. Phys. Chem. C*, 2021, **125**, 4397–4411.
32 L. D. Chen, M. Urushihara, K. Chan and J. K. Nørskov, *ACS Catal.*, 2016, **6**, 7133–7139.
33 G. Hussain, L. Pérez-Martínez, J.-B. Le, M. Papasizza, G. Cabello, J. Cheng and A. Cuesta, *Electrochimica Acta*, 2019, **327**, 135055.
34 S. Ringe, E. L. Clark, J. Resasco, A. Walton, B. Seger, A. T. Bell and K. Chan, *Energy Environ. Sci.*, 2019, **12**, 3001–3014.
35 J. Resasco, L. D. Chen, E. Clark, C. Tsai, C. Hahn, T. F. Jaramillo, K. Chan and A. T. Bell, *J. Am. Chem. Soc.*, 2017, **139**, 11277–11287.
36 M. C. O. Monteiro, F. Dattila, N. López and M. T. M. Koper, *J. Am. Chem. Soc.*, 2022, **144**, 1589–1602.
37 M. C. O. Monteiro, F. Dattila, B. Hagedoorn, R. García-Muelas, N. López and M. T. M. Koper, *Nat. Catal.*, 2021, **4**, 654–662.
38 M. R. Singh, Y. Kwon, Y. Lum, J. W. Ager and A. T. Bell, *J. Am. Chem. Soc.*, 2016, **138**, 13006–13012.
39 B. Endrődi, A. Samu, E. Kecsenovity, T. Halmágyi, D. Sebők and C. Janáky, *Nat. Energy*, 2021, **6**, 439–448.
40 M. C. O. Monteiro, M. F. Philips, K. J. P. Schouten and M. T. M. Koper, *Nat. Commun.*, 2021, **12**, 4943.
41 M. R. Thorson, K. I. Siil and P. J. A. Kenis, *J. Electrochem. Soc.*, 2013, **160**, F69–F74.
42 S. S. Bhargava, F. Proietto, D. Azmoodeh, E. R. Cofell, D. A. Henckel, S. Verma, C. J. Brooks, A. A. Gewirth and P. J. A. Kenis, *ChemElectroChem*, 2020, **7**, 2001–2011.
43 G. Marcandalli, A. Goyal and M. T. M. Koper, *ACS Catal.*, 2021, **11**, 4936–4945.
44 Y.-Q. Wang, X.-H. Dan, X. Wang, Z.-Y. Yi, J. Fu, Y.-C. Feng, J.-S. Hu, D. Wang and L.-J. Wan, *J. Am. Chem. Soc.*, 2022, **144**, 20126–20133.
45 J. Du, A. Fiorani, T. Inagaki, A. Otake, M. Murata, M. Hatanaka and Y. Einaga, *JACS Au*, 2022, **2**, 1375–1382.
46 S. Liu, M. Jin, J. Sun, Y. Qin, S. Gao, Y. Chen, S. Zhang, J. Luo and X. Liu, *Chem. Eng. J.*, 2022, **437**, 135294.
47 T. Sekimoto, M. Deguchi, S. Yotsuhashi, Y. Yamada, T. Masui, A. Kuramata and S. Yamakoshi, *Electrochem. Commun.*, 2014, **43**, 95–97.
48 D. A. Torelli, S. A. Francis, J. C. Crompton, A. Javier, J. R. Thompson, B. S. Brunschwig, M. P. Soriaga and N. S. Lewis, *ACS Catal.*, 2016, **6**, 2100–2104.
49 T. Chen, J. Hu, K. Wang, K. Wang, G. Gan and J. Shi, *Energy Fuels*, 2021, **35**, 17784–17790.
50 Y. Hori and A. Murata, *Electrochimica Acta*, 1990, **35**, 1777–1780.
51 Z. Zhang, J. Zhu, S. Chen, W. Sun and D. Wang, *Angew. Chem. Int. Ed.*, 2023, **62**, e202215136.
52 F. S. Khan, M. Sugiyama, K. Fujii, Yu. S. Tver'yanovich and Y. Nakano, *Heliyon*, 2020, **6**, e03513.
53 N. S. Shaikh, J. S. Shaikh, V. Márquez, S. C. Pathan, S. S. Mali, J. V. Patil, C. K. Hong, P. Kanjanaboos, O. Fontaine, A. Tiwari, S. Praserthdam and P. Praserthdam, *Mater. Today Sustain.*, 2023, 100384.
54 X. Zheng, P. De Luna, F. P. García de Arquer, B. Zhang, N. Becknell, M. B. Ross, Y. Li, M. N. Banis, Y. Li, M. Liu, O. Voznyy, C. T. Dinh, T. Zhuang, P. Stadler, Y. Cui, X. Du, P. Yang and E. H. Sargent, *Joule*, 2017, **1**, 794–805.
55 J. S. Yoo, R. Christensen, T. Vegge, J. K. Nørskov and F. Studt, *ChemSusChem*, 2016, **9**, 358–363.
56 V. S. K. Yadav, Y. Noh, H. Han and W. B. Kim, *Catal. Today*, 2018, **303**, 276–281.
57 X. Bai, W. Chen, C. Zhao, S. Li, Y. Song, R. Ge, W. Wei and Y. Sun, *Angew. Chem.*, 2017, **129**, 12387–12391.
58 Y. Wang, Y. Chen, Y. Zhao, J. Yu, Z. Liu, Y. Shi, H. Liu, X. Li and W. Zhou, *Appl. Catal. B Environ.*, 2022, **307**, 120991.

 

59 B. Ren, G. Wen, R. Gao, D. Luo, Z. Zhang, W. Qiu, Q. Ma, X. Wang, Y. Cui, L. Ricardez–Sandoval, A. Yu and Z. Chen, *Nat. Commun.*, 2022, **13**, 2486.
60 R. Sacci, S. Velardo, L. Xiong, D. Lutterman and J. Rosenthal, *Energies*, 2019, **12**, 3132.
61 B. Kumar, V. Atla, J. P. Brian, S. Kumari, T. Q. Nguyen, M. Sunkara and J. M. Spurgeon, *Angew. Chem. Int. Ed.*, 2017, **56**, 3645–3649.
62 K. Li, S. Zhang, X. Zhang, S. Liu, H. Jiang, T. Jiang, C. Shen, Y. Yu and W. Chen, *Nano Lett.*, 2022, **22**, 1557–1565.
63 X. Sun, Y. Tuo, C. Ye, C. Chen, Q. Lu, G. Li, P. Jiang, S. Chen, P. Zhu, M. Ma, J. Zhang, J. H. Bitter, D. Wang and Y. Li, *Angew. Chem.*, 2021, **133**, 23806–23810.
64 H. Chen, Z. Wang, X. Wei, S. Liu, P. Guo, P. Han, H. Wang, J. Zhang, X. Lu and B. Wei, *Appl. Surf. Sci.*, 2021, **544**, 148965.
65 S. Chen, T. Liu, S. O. Olanrele, Z. Lian, C. Si, Z. Chen and B. Li, *J. Energy Chem.*, 2021, **54**, 143–150.
66 K. Fan, Y. Jia, Y. Ji, P. Kuang, B. Zhu, X. Liu and J. Yu, *ACS Catal.*, 2020, **10**, 358–364.
67 X. Chen, H. Chen, W. Zhou, Q. Zhang, Z. Yang, Z. Li, F. Yang, D. Wang, J. Ye and L. Liu, *Small*, 2021, **17**, 2101128.